Delft University of Technology

Document Version
Final published version

Licence
CC BY

Citation (APA)
Eijkelhof, D., & Schmehl, R. (2022). Six-degrees-of-freedom simulation model for future multi-megawatt airborne wind energy systems. *Renewable Energy*, *196*, 137-150. https://doi.org/10.1016/j.renene.2022.06.094

Important note
To cite this publication, please use the final published version (if applicable).
Please check the document version above.

Copyright
In case the licence states “Dutch Copyright Act (Article 25fa)”, this publication was made available Green Open Access via the TU Delft Institutional Repository pursuant to Dutch Copyright Act (Article 25fa, the Taverne amendment). This provision does not affect copyright ownership.
Unless copyright is transferred by contract or statute, it remains with the copyright holder.

Sharing and reuse
Other than for strictly personal use, it is not permitted to download, forward or distribute the text or part of it, without the consent of the author(s) and/or copyright holder(s), unless the work is under an open content license such as Creative Commons.

Takedown policy
Please contact us and provide details if you believe this document breaches copyrights.
We will remove access to the work immediately and investigate your claim.

This work is downloaded from Delft University of Technology.

Renewable Energy 196 (2022) 137–150

Contents lists available at ScienceDirect

Renewable Energy

journal homepage: www.elsevier.com/locate/renene

Six-degrees-of-freedom simulation model for future multi-megawatt airborne wind energy systems

Dylan Eijkelhof *, Roland Schmehl

Delft University of Technology, Faculty of Aerospace Engineering, Kluyverweg 1, 2629 HS, Delft, the Netherlands

ARTICLE INFO

Article history:
Received 3 January 2022
Received in revised form
16 June 2022
Accepted 18 June 2022
Available online 1 July 2022

Keywords:
Airborne wind energy
Airborne wind energy systems
Tether model
Reference model
6 DoF rigid body kite
Airborne wind energy power performance

ABSTRACT

Currently developed airborne wind energy systems have reached sizes of up to several hundred kilowatts. This paper presents the high-level design and a six-degrees-of-freedom model of a future fixed-wing airborne wind energy system operated in pumping cycles. This framework is intended to be used as an open-source reference system. The fixed-wing aircraft has a span of 42.5 m and produces a nominal electrical power of 3 MW. The ground station is modelled as a winch with a rotational degree of freedom describing the reel-in and reel-out motion, constant drum diameter and drive train inertia. A quasi-static approach is used to model the relatively stiff tether. The tether is discretised by 16 segments with variable length to account for reeling. A tracking controller ensures the kite's flight path during the autonomous pumping cycle operation. The controller alternates between crosswind figure-of-eight manoeuvres while reeling out and gliding on an arc-shaped path towards the ground station during retraction. The operational and controller parameters are determined using a CMA-ES evolution algorithm to maximise the average cycle power of a specific kite design at different wind speeds and given operational constraints. The algorithm identifies optimised flight paths for a range of wind speeds up to 30 m s^{-1} leading to a power curve with a cut-in wind speed of 10 m s^{-1} at operating altitude.

© 2022 The Authors. Published by Elsevier Ltd. This is an open access article under the CC BY license (http://creativecommons.org/licenses/by/4.0/).

1. Introduction

Airborne wind energy (AWE) converts wind energy into electricity using tethered flying devices. A representative selection of currently developed AWE systems is illustrated in Fig. 1 [1–4]. Weiss [5] provides a general overview of AWE technology's current industry trends, which are in the power range up to several hundred kilowatts. These systems can be classified into ground- and on board generation (Ground-Gen and Fly-Gen) but also into soft and fixed-wing kite systems [6]. Ground-Gen systems generate electricity on the ground where the mechanical power from a reeling tether is converted into electrical power. Fly-Gen systems generate electricity directly on board by means of installed small turbines. For the envisioned scaling step towards megawatts, computational tools for the simulation of the entire AWE system, covering all relevant physics, will be indispensable. Linearly increasing the kite dimensions will increase the mass of the structure. Soft kites commonly have the benefit that added volume is mostly extra air trapped by the flexible membrane, thus only a little increase in mass. However, for fixed-wing kites, increasing dimensions can cause severe implications to the operation due to its added weight. A quadratic increase of the wing area will approximately scale the volume(i.e. mass) cubically. This is known as the square-cube law [7]. The unfavourably increasing mass of the kite negatively affects the tension on the tether, which in turn reduces the expected power increase of the larger system. Increasing inertia also reduces the controllability, which can cause complications during transition phases, for example. Another important reason why the industry will rely more and more on more accurate computational tools is the cost that comes with testing. The larger the system becomes, the higher the cost to build and test the design.

A complete AWE system simulation tool already exists for Fly-Gen systems. Larco and Echeverri [8] published the source code of a flight simulator of the Makani M600 energy kite, with a 26 m wing span and eight on board wind turbines. The kite is modelled as a rigid body, 6 Degrees-of-freedom (DoF) dynamics, with aerodynamic look-up tables dependent on the angle of attack and sideslip angle. Wijnja et al. [9] presented a computational aeroelastic analysis of this system, including wind tunnel experiments of a small-scale model of the main wing, to assess the influence of

* Corresponding author.
E-mail address: d.eijkelhof@tudelft.nl (D. Eijkelhof).

https://doi.org/10.1016/j.renene.2022.06.094
0960-1481/© 2022 The Authors. Published by Elsevier Ltd. This is an open access article under the CC BY license (http://creativecommons.org/licenses/by/4.0/).

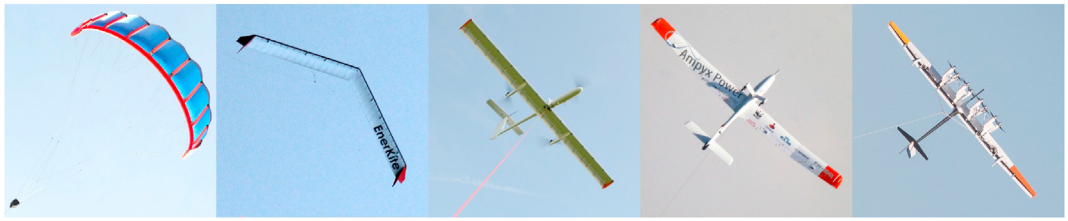

Fig. 1. Selection of AWE systems in development: Kitepower, EnerKíte, TwingTec, Ampyx Power and Makani Power (from left to right), generating up to 600 kW per single system.

the bridle line attachment points. Bauer [10] presented a multi-disciplinary steady systems engineering model for the analysis of on board generation AWE systems and validated this against the power curve of the small-scale Makani Wing 7, among others.

This research focuses on Ground-Gen systems rather than the Fly-Gen systems. Important previous and ongoing developments that lay the foundation of the present work, are the following. Williams [11] summarises discretised tether models and introduces the quasi-static model of a discretised tether. Licitra et al. [12,13] present a dynamic model of the Ampyx Power AP-3 (12 m^2 wing area) aircraft. Rapp et al. [14,15] present the dynamic model and flight control framework underlying also the present work. Eijkelhof [16] shows the detailed design process of a large-scale reference kite for a Ground-Gen system. The kite design is inspired by the configuration of the Ampyx Power AP-3 but scaled up to a 150 m^2 wing surface area like the envisioned design of the Ampyx Power AP-4. The AP-4 will be developed to enter the market of large-scale energy generation [17]. Malz et al. [18] introduce a reference model based on the Ampyx Power AP-2 (3 m^2 wing area). Rapp and Schmehl [19] use this model to enhance the resilience of an AWE system against perturbations. Eijkelhof et al. [20] present a point mass model of the multi-megawatt airborne wind energy system designed in Ref. [16]. Malz et al. [21] present an optimal control problem (OCP) formulation of AWE operation and in Ref. [22] they present a limit value analysis of AWE in the European wind energy market.

The paper is structured as follows. Section 2 describes the computational model, elaborating on the 6 DoF model of the kite, the control system, the quasi-static discretised tether, wind shear and the optimisation strategy. Section 3 gives a detailed description of the reference system. Section 4 presents the results of one cycle during continuous pumping cycle operations at 22 m s^{-1} wind. Section 5 concludes this research and Section 6 shows the location of the open-source simulation framework developed throughout the present work.

2. Computational model

A simplified schematic of how the different sub-components of the model work together to simulate continuous operation in pumping cycles is shown in Fig. 2.

First, the model is initialised in Matlab before switching to the Simulink environment. At the start of the simulation, the initialised kite velocity and position together with the tether force at the ground form the flight state vector $\boldsymbol{X}$. The dynamic state vector $\boldsymbol{y}$ is given by the kinetic velocity and angular velocity around the kite's centre of gravity. Both $\boldsymbol{X}$ and $\boldsymbol{y}$ are passed to the controller, to the aerodynamic, the ground station and the tether module and finally, to the time integration.

The flight controller, described in Section 2.2, enables the tethered kite to follow predefined trajectories. Doing so, it sets the desired actuator inputs $\boldsymbol{C}_{act}$ for the kite and the ground controller inputs $\boldsymbol{C}_T$ for the ground station. In the aerodynamic module, the

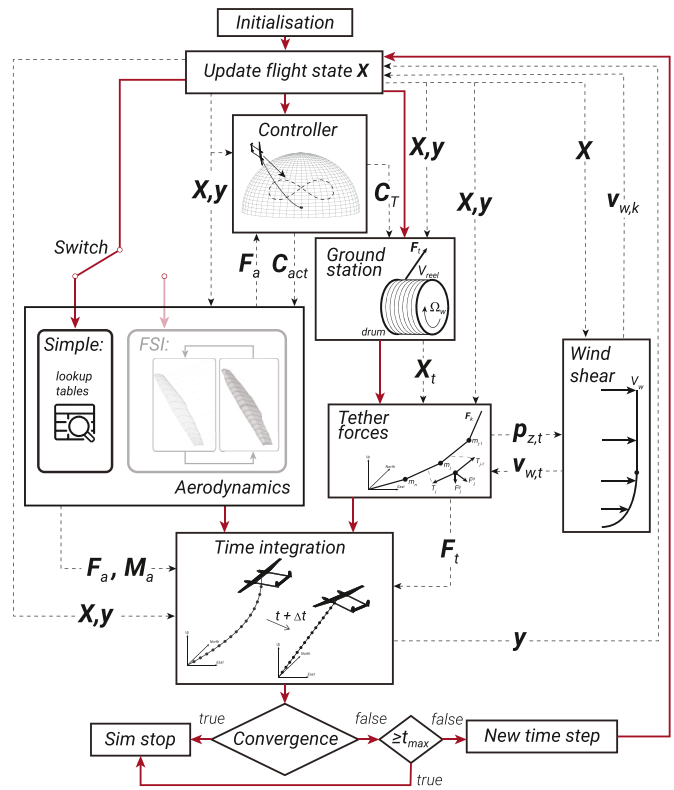

Fig. 2. Simulation model flowchart with flight state vector $\boldsymbol{X}$ and dynamic state vector $\boldsymbol{y}$.

forces and moments $\boldsymbol{F}_a$ and $\boldsymbol{M}_a$ acting on the drone are determined. This could be done by either predefined look-up tables as used in this work or with an FSI algorithm.

The mechanical power produced by the system is determined in the ground station module. This module updates the parameters required by the tether module in $\boldsymbol{X}_T$. The winch control strategy is further explained in Section 2.3.

The tether loads are determined by the tether module shown in Section 2.4. The shape of the tether and the loads acting at ground station $\boldsymbol{F}_t$ and the kite $\boldsymbol{F}_{t,\,k}$ are assessed.

The wind shear module, described in Section 2.5, calculates the wind speed at a given altitude for both tether particles $\boldsymbol{V}_{w,\,t}$ at altitudes $\boldsymbol{p}_{z,\,t}$ and at the kite $\boldsymbol{V}_{w,\,k}$.

Finally, the calculated aerodynamic and tether loads and moments are passed to the time integration. The dynamic state vector y is then advanced. The time derivatives of the kite's dynamic states are given in Section 2.1. If convergence, as described in Section 4.1, occurs or the maximum simulation time is exceeded, the simulation stops. If neither of these two take place, the flight state is updated, and the next iteration is initialised.

The source code of the implemented model is available from Ref. [23].

2.1. Kite equations of motion

Standard 6 DoF rigid body equations of motion (EoM) in the body-fixed reference frame, assuming a flat-non-rotating earth, are presented in Equations (1) and (2). An additional force term appears in the translational equations visible in Equation (3). A full derivation of these equations can be found in Ref. [24]. The tether is attached in the centre of gravity, thus does not affect the three rotational EoM.

$$\dot{\boldsymbol{V}}_{\mathrm{k}}^{\mathrm{B}} = \frac{1}{m}\boldsymbol{F}_{\mathrm{tot}} - \boldsymbol{\omega} \times \boldsymbol{V}_{\mathrm{k}}, \tag{1}$$

$$\dot{\boldsymbol{\omega}}^{\mathrm{B}} = \boldsymbol{J}^{-1}[\boldsymbol{M} - \boldsymbol{\omega} \times (\boldsymbol{J}\boldsymbol{\omega})], \tag{2}$$

$$\boldsymbol{F}_{\mathrm{tot}} = \boldsymbol{F}_{\mathrm{aero}} + \boldsymbol{F}_{\mathrm{tether}} + \boldsymbol{F}_{\mathrm{g}} + \boldsymbol{F}_{\mathrm{prop,\ brake}}, \tag{3}$$

$$\boldsymbol{J} = \begin{bmatrix} J_{xx} & 0 & 0 \\ 0 & J_{yy} & 0 \\ 0 & 0 & J_{zz} \end{bmatrix}, \tag{4}$$

where $\dot{\boldsymbol{V}}_{\mathrm{k}}^{\mathrm{B}}$ and $\boldsymbol{V}_{\mathrm{k}}$ are the kinetic acceleration and velocity, respectively, $\boldsymbol{F}_{\mathrm{tot}}$ is the sum of forces acting on the kite (given by Equation (3)), $\dot{\boldsymbol{\omega}}^{\mathrm{B}}$ and $\boldsymbol{\omega}$ are the angular acceleration and velocity, respectively, around the centre of gravity, $\boldsymbol{M}$ is the sum of moments acting on the kite and $\boldsymbol{J}$ the inertia matrix, given by Equation (4). The kinetic velocity is defined by Equation (5).

$$\boldsymbol{V}_{\mathrm{k}} = \boldsymbol{V}_{\mathrm{w}} - \boldsymbol{V}_{\mathrm{a}}, \tag{5}$$

where $\boldsymbol{V}_{\mathrm{a}}$ is the apparent wind velocity and $\boldsymbol{V}_{\mathrm{w}}$ is the wind velocity.

Conversion between reference frames can be done by using two rotation matrices. The rotation matrix from body-fixed(B) to inertial(O) reference frame is given by Equation (6).

$$\boldsymbol{R}_{\mathrm{OB}} = [\boldsymbol{r}_{\mathrm{OB}_1}, \boldsymbol{r}_{\mathrm{OB}_2}, \boldsymbol{r}_{\mathrm{OB}_3}], \tag{6}$$

with column vectors given by:

$$\boldsymbol{r}_{\mathrm{OB}_1} = \begin{bmatrix} \cos\psi\cos\theta \\ \sin\psi\cos\theta \\ -\sin\theta \end{bmatrix},$$

$$\boldsymbol{r}_{\mathrm{OB}_2} = \begin{bmatrix} \cos\psi\sin\theta\sin\varphi - \sin\psi\cos\varphi \\ \sin\psi\sin\theta\sin\varphi + \cos\psi\cos\varphi \\ \cos\theta\sin\varphi \end{bmatrix},$$

$$\boldsymbol{r}_{\mathrm{OB}_3} = \begin{bmatrix} \cos\psi\sin\theta\cos\varphi + \sin\psi\sin\varphi \\ \sin\psi\sin\theta\cos\varphi - \cos\psi\sin\varphi \\ \cos\theta\cos\varphi \end{bmatrix},$$

where φ, θ and ψ are the three Euler angles. The rotation matrix from inertial(O) to wind(W) reference frame is shown by Equation (7).

$$\boldsymbol{R}_{\mathrm{WO}} = \begin{bmatrix} \cos\pi & \sin\pi & 0 \\ \sin\pi & -\cos\pi & 0 \\ 0 & 0 & -1 \end{bmatrix}. \tag{7}$$

2.2. Flight control and flight path planning

In the following, a concise description of the utilised control system is given. For a detailed derivation, please refer to Refs. [14,25]. Both inner and outer loop of the controller need to be used. The inner loop is responsible for the determination of the actuator inputs and the outer loop for calculating the required roll, pitch and yaw angles. The flight controller needs to guide the aircraft along a defined figure of eight flight path during the traction phase and a vertical arc back during the retraction phase. During the traction phase the required course and path angle rates $\dot{\chi}_{\mathrm{k,\ c}}$ and $\dot{\gamma}_{\mathrm{k,\ c}}$ are directly calculated based on the optimised path curvature as well as the current relative position of the aircraft with respect to the path. During the retraction phase desired course and path angles are based on the error with respect to the prescribed retraction path. The reference angles are first passed through a second-order reference filter (illustrated in Fig. 3) to smoothen the change in values over time, similar to the figure of eight guidance. The limits and ω_0 values are controller parameters specific for each input parameter, and ζ_0 is assumed to be 1.

The required angle of attack, α_{a} and roll angle, μ_{a} are calculated by inverting the path dynamics, which in turn determines the necessary manoeuvre forces to follow the prescribed directions. These reference angles are then tracked by the inner loop to determine the required actuator deflections. First, the attitude controller uses dynamic inversion to determine the angular rates of the aircraft and then the rate controller calculates the required change in moments. The aileron (δ_{a}), elevator (δ_{e}) and rudder (δ_{r}) deflections can then be determined using Equation (8).

$$\begin{bmatrix} \delta_{\mathrm{a}} \\ \delta_{\mathrm{e}} \\ \delta_{\mathrm{r}} \end{bmatrix} = \frac{1}{\bar{q}A} \begin{bmatrix} \frac{1}{b} & 0 & 0 \\ 0 & \frac{1}{\bar{c}} & \\ 0 & 0 & \frac{1}{b} \end{bmatrix} \boldsymbol{B}_{\mathrm{a}}^{-1} \boldsymbol{M}_{a,\delta}, \tag{8}$$

where $\bar{q}$ is the dynamic pressure, A the wing surface area, b the wing span, $\bar{c}$ the average wing chord, $\boldsymbol{B}_a$ the pre-computed control allocation matrix given in Equation (9) and $\boldsymbol{M}_{a,\delta}$ the required roll pitch and yaw moment increments.

$$\boldsymbol{B}_{\mathrm{a}} = \begin{bmatrix} C_{\mathrm{l}_{\delta_{\mathrm{a}}}}(\alpha_{\mathrm{a}}) & 0 & C_{\mathrm{l}_{\delta_{\mathrm{r}}}}(\alpha_{\mathrm{a}}) \\ C_{\mathrm{m}_{\delta_{\mathrm{a}}}}(\alpha_{\mathrm{a}}) & C_{\mathrm{m}_{\delta_{\mathrm{e}}}}(\alpha_{\mathrm{a}}) & 0 \\ 0 & 0 & C_{\mathrm{n}_{\delta_{\mathrm{r}}}}(\alpha_{a}) \end{bmatrix}, \tag{9}$$

where C_l, C_m, C_n are the roll, pitch and yaw coefficients, respectively and calculated using Equations (10)–(12).

$$C_{\mathrm{l}} = \frac{L}{0.5\rho V^2 A b}, \tag{10}$$

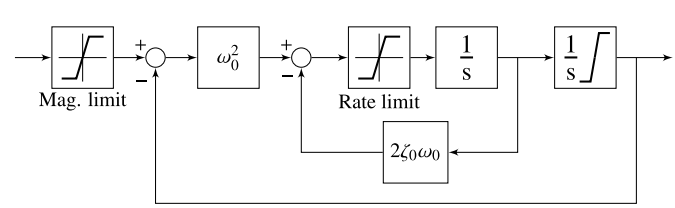

Fig. 3. Second-order reference filter.

$$C_m = \frac{M}{0.5\rho V^2 Ac}, \tag{11}$$

$$C_n = \frac{N}{0.5\rho V^2 Ab}, \tag{12}$$

where L, M and N are the roll, pitch and yaw moments, respectively.

For each, the derivatives with respect to the aileron, elevator and rudder deflections are determined by assuming a linear relation between coefficient and deflection. This value is then calculated at different angles of attack (α_a), and a second-order polynomial is fitted to the outcome, given by Equations (13)–(17) for the reference kite described in Section 3.

$$C_{l_{\delta_a}}(\alpha_a) = -0.1704\alpha_a^2 - 0.0816\alpha_a + 0.1572, \tag{13}$$

$$C_{l_{\delta_r}}(\alpha_a) = -0.0090\alpha_a^2 + 0.0091, \tag{14}$$

$$C_{m_{\delta_a}}(\alpha_a) = 0.0130\alpha_a^2 + 0.0150\alpha_a + 0.0125, \tag{15}$$

$$C_{m_{\delta_e}}(\alpha_a) = 6.9679\alpha_a^2 - 0.0076\alpha_a - 1.9224, \tag{16}$$

$$C_{n_{\delta_r}}(\alpha_a) = -0.0763\alpha_a^2 + 0.0767. \tag{17}$$

Finally, at each time step in the simulation, the control allocation matrix is then reconstructed from the pre-computed polynomial coefficients and the current angle of attack. This is found to be sufficient to control the aircraft. Nonetheless, the better these values represent the actual aircraft response, the better the controller can predict the outcome and act accordingly. All values are determined using the same approach as done for the aerodynamic coefficients in Section 3.3, using the FSI algorithm from Ref. [26].

Each commanded deflection is then passed through a first order reference filter (illustrated in Fig. 4), with rate and position limits to give the actual deflections. The first order reference filter has similar bandwidth (5.6 Hz) and rate limits (2 rad s^{-1}) for the ailerons, elevator and rudders.

2.3. Winch controller

The winch controller is a simplified version of the controller introduced by Rapp et al. [14]. The reference torque is determined by a PI controller where the input is the error between tether force set point and the measured tether force at the ground station. Although this simplification leads to less accurate force tracking, the PI controller yields a more robust performance if winch acceleration limits are taken into account.

2.4. Tether model

A quasi-static lumped-mass tether model is implemented based on [11]. This allowed the tether to be modelled at full stiffness of Dyneema® while keeping a simulation time step large enough for fast simulations. The main assumption is that elastic vibrations are neglected. An entirely dynamic simulation would require a very small time step to capture the dynamics of a stiff tether material. In Ref. [20] such an entirely dynamic tether model is used based on a spring-damper lumped mass approach. However, the tether uses a non-real (much lower) stiffness to reduce computational effort raising questions about the validity of the results.

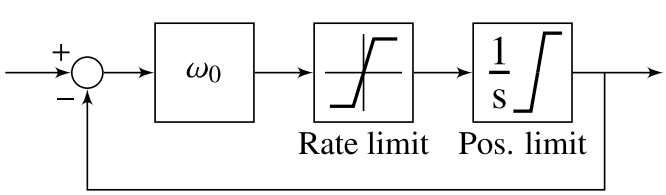

Fig. 4. First-order reference filter.

The quasi-static approach computes the steady state shape and corresponding tension forces throughout the tether by means of a shooting process starting at the ground station towards the kite (a summary of this can be found in Ref. [11]). The shape is then a result of an equilibrium between centrifugal forces coming from the tether rotation and present external forces. The dominating forces acting on the tether are assumed to be gravity and drag. The tether length, wind speed at each discretisation mass, kite velocity and position are known at each time step. A Trust-Region Dogleg Method, adapted from the approach implemented by MathWorks Inc. in Matlab R2019B [27], alternates the tether force and direction at the ground station until the tether end is coincident with the kite position (determined through a separate integration process). Coincident means a magnitude of less than 1×10^{-6} for the distance between the two. The state vector is given by $[\theta_n,\ \varphi_n,\ T_n]^T$ with the tension force in the wind reference frame at the ground station given by $\boldsymbol{T}_n = T_n[\sin\theta_n\cos\varphi_n,\ \sin\varphi_n,\ \cos\theta_n\cos\varphi_n]^T$. Even though [11] mentions other state vectors can be used instead (e.g. three Cartesian coordinates), the spherical coordinates make it possible to limit the solution to a positive definite force magnitude (i.e. no compression) with arbitrary direction, as the magnitude is one of the state parameters. This makes the implemented Trust-Region Dogleg Method much more stable and establishes fast convergence. However there might be algorithms that are more stable and faster that were not tested in this work. Williams [11] uses a C version of the cminpack solver in Netlib, but a complete framework written solely in Matlab is preferred (Simulink does compile the Matlab code into C for faster run-time). Fig. 5 shows the discretisation of the tether in a number of particle masses and the force equilibrium at each mass. The detailed tether characteristics used during all simulations are given in Table 1.

The equations of motion are given by Equation (18) for discretised mass.

$$m_j\ddot{\boldsymbol{p}}_j = \boldsymbol{T}_{j-1} - \boldsymbol{T}_j - \boldsymbol{F}_j^g + \boldsymbol{F}_j^d, \tag{18}$$

where $\boldsymbol{F}_j^g$ and $\boldsymbol{F}_j^d$ are the external gravitational and drag forces,

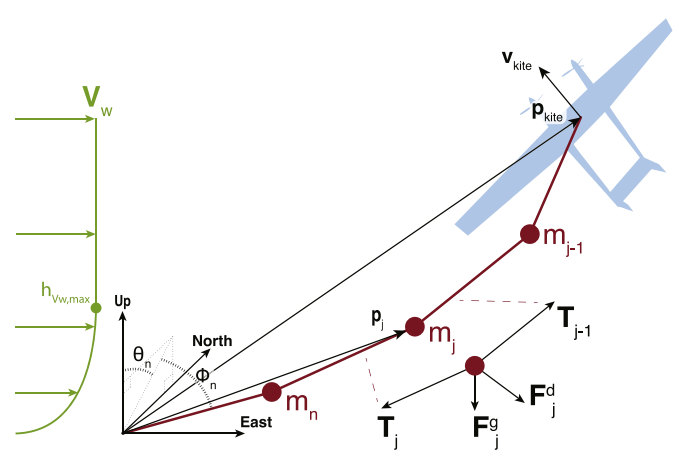

Fig. 5. Discretisation and force equilibrium of the tether exposed to a vertical wind profile given in the wind reference frame.

Table 1
Detailed tether characteristics.

Parameter	Value	Unit
Diameter (d)	0.0297	m
Linear density (ρ_t)	0.6729	kg m^{-1}
Normal drag coefficient (C_N)	1.2	-
Axial elastic modulus (E)	116×10^9	GPa
Number of masses (N_p)	15	-

respectively. The dominating external forces are given by Equations (20) and (21). $\ddot{\boldsymbol{p}}_j$ is the acceleration of the particle assumed to be only the centrifugal component calculated from Equation (19) and m_j is the particle mass.

$$\ddot{\boldsymbol{p}}_{\mathrm{j}} = \left(\frac{\boldsymbol{p}_{\mathrm{kite}}}{\mathrm{norm}\ \boldsymbol{p}_{\mathrm{kite}}{}^2} \times \boldsymbol{v}_{\mathrm{kite}}\right) \times \left[\left(\frac{\boldsymbol{p}_{\mathrm{kite}}}{\mathrm{norm}\ \boldsymbol{p}_{\mathrm{kite}}{}^2} \times \boldsymbol{v}_{\mathrm{kite}}\right) \times \boldsymbol{p}_{\mathrm{j}}\right], \tag{19}$$

$$\boldsymbol{F}_{\mathrm{j}}^{\mathrm{g}} = [0,\ 0,\ m_{\mathrm{j}}g]^{\mathrm{T}}, \tag{20}$$

$$\boldsymbol{F}_{\mathrm{j}}^{\mathrm{d}} = -\frac{1}{2}\rho_{\mathrm{t}}L_{\mathrm{j}}dC_{\mathrm{N}}\mathrm{norm}\ \boldsymbol{v}_{\mathrm{j}}^{\mathrm{n}}\boldsymbol{v}_{\mathrm{j}}^{\mathrm{n}}, \tag{21}$$

where $\boldsymbol{p}_{kite}$ and $\boldsymbol{v}_{kite}$ are the position and velocity of the kite, respectively, ρ_t is the linear density, L_j the unstrained segment length, d the diameter and C_N the normal drag coefficient of the tether. $\boldsymbol{v}_j^r$ is the relative wind velocity at each segment with its normal ($\boldsymbol{v}_j^n$) and tangent ($\boldsymbol{v}_j^t$) component computed by Equations (22)–(24).

$$\boldsymbol{v}_{\mathrm{j}}^{\mathrm{t}} = \left(\frac{\boldsymbol{p}_{\mathrm{j-1}} - \boldsymbol{p}_{\mathrm{j}}}{\mathrm{norm}\ \boldsymbol{p}_{\mathrm{j-1}} - \boldsymbol{p}_{\mathrm{j}}} \cdot \boldsymbol{v}_{\mathrm{j}}^{\mathrm{r}}\right) \frac{\boldsymbol{p}_{\mathrm{j-1}} - \boldsymbol{p}_{\mathrm{j}}}{\mathrm{norm}\ \boldsymbol{p}_{\mathrm{j-1}} - \boldsymbol{p}_{\mathrm{j}}}, \tag{22}$$

$$\boldsymbol{v}_{\mathrm{j}}^{\mathrm{n}} \triangleq \boldsymbol{v}_{\mathrm{j}}^{\mathrm{r}} - \boldsymbol{v}_{\mathrm{j}}^{\mathrm{t}}, \tag{23}$$

$$\boldsymbol{v}_{\mathrm{j}}^{\mathrm{r}} = \boldsymbol{v}_{\mathrm{j}} - \boldsymbol{V}_{\mathrm{w,\ j}}, \tag{24}$$

where $\boldsymbol{V}_{w,j}$ is the wind speed at particle height.

Equation (18) can be used to calculate $\boldsymbol{T}_{j-1}$ from $\boldsymbol{T}_j$ in the shooting process up to the kite attachment point, knowing the external forces and particle acceleration. Assuming Hooke's law the position of m_{j-1} can be determined using Equations (25) and (26).

$$l_{\mathrm{j-1}} = \left(\frac{\mathrm{norm}\ \boldsymbol{T}_{\mathrm{j-1}}}{EA} + 1\right)L_{\mathrm{j}}, \tag{25}$$

$$\boldsymbol{p}_{\mathrm{j-1}} = \boldsymbol{p}_{\mathrm{j}} + l_{\mathrm{j-1}}\frac{\boldsymbol{T}_{\mathrm{j-1}}}{\mathrm{norm}\ \boldsymbol{T}_{\mathrm{j-1}}}, \tag{26}$$

where l_{j-1} is the strained segment length, E the axial elastic modulus and A the cross-sectional area.

2.5. Wind field

For accurate power predictions, it is important to know how the wind speed varies with altitude would be. A common assumption for conventional wind energy applications is a logarithmic wind speed profile [28]. This profile is generally suitable up to an altitude of 200 m. As airborne wind energy systems operate in higher altitudes, the logarithmic profile is not valid anymore. Therefore it is chosen to use a reference site with a measured wind profile to represent the variation with altitude during all simulations presented in this paper. The reference site is chosen to be the Ijmuiden offshore wind speed measurement tower, taking the average wind speed profile given in Ref. [29]. The profile is normalised by the maximum wind speed and can thus be scaled to each operational wind speed of the power curve. As this is offshore wind, the wind speeds vary less with altitude than an onshore location (e.g. Cabauw wind measurement tower). As the measured wind speeds only go as high as 600 m altitude it is assumed that the wind speed stays constant from the altitude where the maximum wind speed was measured. For Ijmuiden the maximum occurs at 250 m altitude. This approach allows the optimisation algorithm to freely change the height where the system will operate under specific wind conditions. This assumption seems reasonably valid as the influence of the earth surface is negligible above the atmospheric boundary layer. LIDAR measurements performed by Sommerfeld [30] show similar behaviour. Another approach could be to use the entire measured wind profile and limit the operational altitude to 600 m. Fig. 6 represents the normalised average wind profile of Ijmuiden and Cabauw. Cabauw is then disregarded throughout the rest of this work and the wind shear for Ijmuiden is applied.

2.6. Optimisation strategy

The maximum average pumping cycle power is used as the main objective during all optimisations. The parameters chosen to be varied are shown in Table 2. A Covariance Matrix Adaptation Evolution Strategy (CMA-ES) optimisation method [31] evolves the parameters between each optimisation step by minimising a given objective. A relatively short list of variables is chosen to keep the optimisation time down and these were found to have the most influence on the pumping cycle convergence and power outcome. However, the framework allows for an arbitrary number of system parameters to be optimised. For the full set of simulation parameters, one may refer to the dataset [32] Matlab file "initAllSimParams_DE2019.m". Please note that even though an optimisation is

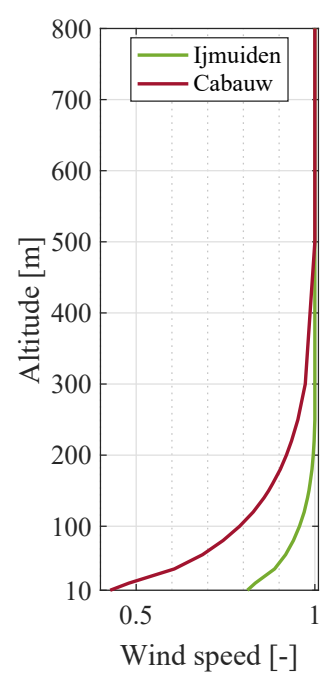

Fig. 6. Vertical wind speed profile normalised to the maximum occurring wind speed, which is at 250 m altitude ($V_{w,\ 250}$) for Ijmuiden and at 500 m altitude ($V_{w,\ 500}$) for Cabauw. Only Ijmuiden is used throughout this work.

Table 2
Operational and controller parameters varied during optimisations.

Controller	Flight path	Tether
K_p winch	Figure-8 roundness	Traction force
K_i winch	Figure-8 width	Retraction force
K_{p,μ_a}	Elevation ∠	Tether length min.
K_{p,α_a}	Transition elevation ∠	Tether length max.
$K_{p,\chi}$ traction	Initial elevation ∠	
$K_{p,\gamma}$ traction	Retraction arc radius	
$K_{p,\chi}$ retraction		
$K_{p,\gamma}$ retraction		
$K_{i,\chi}$ retraction		
$K_{i,\gamma}$ retraction		
K_p roll		
K_p pitch		
K_p yaw		
ω_0 roll		
ω_0 pitch		
ω_0 yaw		
$\omega_{0,\chi}$ retraction		
K_p brake		
K_i brake		

performed, the goal of this research was not the arrive at an optimal controller configuration and flight path. The optimisation can therefore also be seen as a sub-optimised design space exploration of controller parameters and flight path shapes.

The algorithm follows a specific objective. Several penalties are applied in order to steer the evolution of variables in the desired direction. The simulation is terminated when violating the maximum allowable tether force (F_t). Penalties are applied for:

- Exceeding the maximum angle of attack (α_a)
- Exceeding the maximum sideslip angle (β)
- Flying too far from the desired trajectory,
  - Distance during retraction (ε_γ)
  - Distance during traction (Cross-track error) (ε_c)
- Having a too high maximum cycle apparent wind speed (V_a)
- Aggressiveness of the winch in terms of accelerations (a_{winch})

These penalties are then added to minus the average produced power (P_{avg}). The cost function (C) is given by Equation (27)and applies only to logged signals from the last pumping cycle before the convergence criteria is met (see Section 4.1). The optimisation strategy is an objective minimisation problem, hence the minus sign in front of the average power. When no convergence occurs, the power is determined by the total time simulated, the number of pumping cycles performed and the accuracy in following the prescribed flight path. To this power a total error of 7×10^7 is then applied.

$$C = p_{(\varepsilon_{\gamma-xy},\varepsilon_{\gamma-z},\varepsilon_c)} + p_\beta + p_{\alpha_a} + p_{V_a} + p_{W_{Acc}} - P_{avg}, \tag{27}$$

with

$$\begin{aligned} p_{(\varepsilon_{\gamma-xy},\varepsilon_{\gamma-z},\varepsilon_c)} &= 10^3 \cdot \{\max(\max(\varepsilon_{\gamma-xy})/100\text{m} - 1, 0) \\ &\quad + \max(\max(\varepsilon_{\gamma-z})/150\text{m} - 1, 0) \\ &\quad + \max(\max(\varepsilon_c)/150\text{m} - 1, 0)\} \\ p_\beta &= 10^3 \cdot \max(\max(\beta)/20^\circ - 1, 0) \\ p_{\alpha_a} &= 10^6 \cdot \max(\max(\alpha_a)/4.2^\circ - 1, 0) \\ p_{V_a} &= 10^2 \cdot \max\left(\max(V_a)\big/90\text{ms}^{-1}, 0\right) \\ p_{W_{Acc}} &= 10^3 \cdot Var(a_{winch}) \\ P_{avg} &= Mean(P) \end{aligned}$$

3. Reference system

The tethered kite design is detailed in this section. Fig. 7 is a 3D render of the kite (only for illustrative purposes). The key features of this design are presented here accompanied by their design choices. A more comprehensive description of the design process is given by Ref. [16].

The prospective size of the Ampyx Power AP-4 kite formed the basis of the design of this reference system [33,34]. However, at the time, the AP-4 kite was not yet designed and thus the planform of the AP-3 kite was taken [35] as an inspiration instead. This lead to the choice of using a twin-fuselage configuration, which allows for a split of the required propulsion power during take-off (and landing) between the front of each fuselage. The tether attachment point has also been taken similar to the AP-3 kite. The single tether is connected near the kite's centre of gravity, between the fuselages, directly under the main wing. Even though multiple tethers can provide a beneficial amount of redundancy, the loss in power due to an increase in tether drag outweighs drives the choice for only one tether. Adding multiple tether to the system would also add additional complexity and extra material and maintenance costs, increasing the energy price, which is a disadvantage on the economic market [17].

An illustration of the wing and its primary dimensions are shown in Fig. 8. Table 3 gives a brief summary of the planform parameters of the main wing, fuselages, tail and tether.

In Section 3.1, the airframe layout is further discussed. In Section 3.2, the wing skin layup is given, which properties were needed during the kite design phase but not in the simulations of this work as no aeroelastic analysis is performed. However, the predefined lookup tables are determined using an aeroelastic (FSI) algorithm, which needs the structural characteristics of the wing as an input. In Section 3.3, the kite aerodynamic properties are provided.

3.1. Airframe layout

The centre of gravity in Table 3 is in the body-fixed reference frame (Fig. 8). The wing span is chosen in such a way that, combining it with two different chord lengths at the root and tip, an approximate wing surface area of 150 m^2 could be achieved at an aspect ratio of 12. The span and chord lengths were then fixed throughout the rest of the design process. The front and back spar positions and the number of ribs were determined by initial optimisations to maximise the wing load factor (i.e. the buckling failure load divided by weight). The ailerons are sized based on the approach in Ref. [36]. The ailerons extend from 60 to 90% of the half-span. The 10% at the wing tip is not used for the aileron as the tip vortices would provide little control effectiveness. Historical

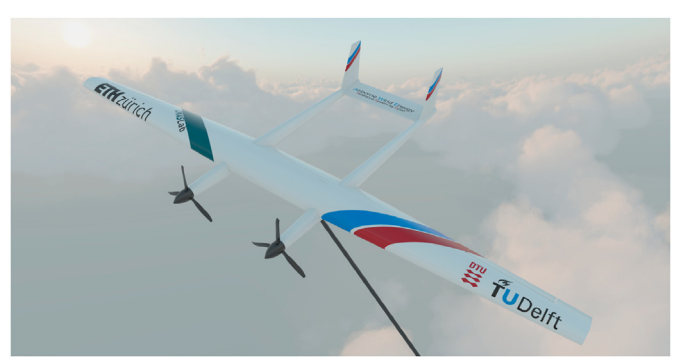

Fig. 7. Rendering of the airborne component of the MegAWES large scale airborne wind energy system.

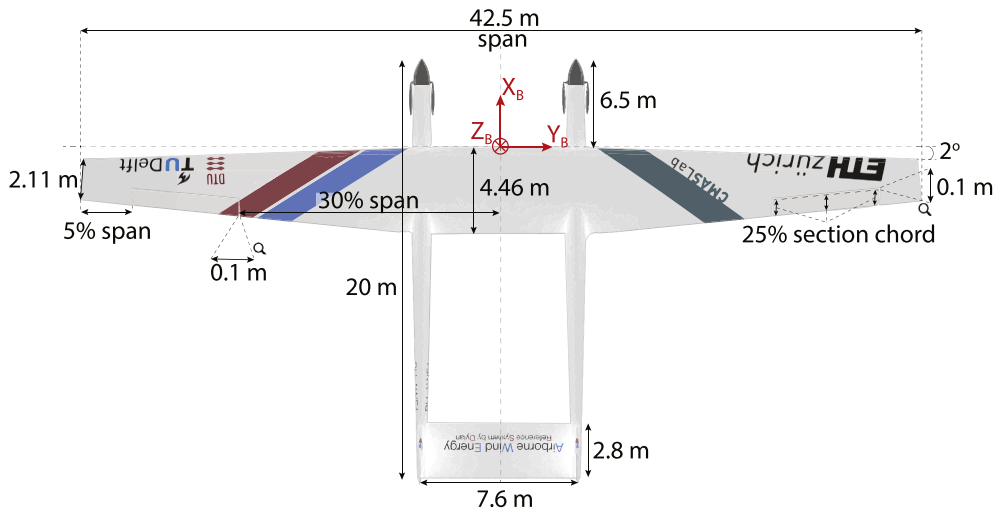

Fig. 8. Planform of the kite.

Table 3
General planform parameters of the wing, tail and fuselage.

Parameter	Value	Unit
Centre of gravity	−1.67, 0, 0.229	m,m,m
Inertia J_{xx}	5.7680×10^5	kg m^2
Inertia J_{yy}	0.8107×10^5	kg m^2
Inertia J_{zz}	6.5002×10^5	kg m^2
Total aircraft mass	6885.2	kg
Wing:		
Span	42.47	m
$Chord_{root}$	4.46	m
$Chord_{tip}$	2.11	m
LE sweep	2	°
Aspect ratio	12.0	-
Surface area	150.45	m^2
$Airfoil_{root}$	$RevE_{HC}$ [16]	
$Airfoil_{tip}$	$RevE_{HC}$ [16]	
Front spar	33.3	% c_{local}
Back spar	43.4	% c_{local}
$Aileron_{root\text{-}inner\ rib}$	60	% $b_{\frac{1}{2}}$
$Aileron_{root\text{-}outer\ rib}$	90	% $b_{\frac{1}{2}}$
$Aileron_{LE\text{-}spar}$	75	% c_{local}
Number of composite ribs	46 (+2 wingtips)	-
$Twist_{root}$ ($Y_{B,+}$ rotation)	5	°
$Twist_{tip}$ ($Y_{B,+}$ rotation)	0	°
Horizontal tail/Elevator:		
Span	7.6	m
Chord	2.8	m
Airfoil	NACA 0012	
Vertical tail/Rudder:		
Span	3	m
Chord	2.8	m
Airfoil	NACA 0012	
Fuselages:		
Length	20	m
Radius	0.6	m
$X_{Nose-LE_{wing}}$	6.5	m
$Y_{Root\text{-}Fuselage}$	3.8	m

guidelines on the aileron chord length show that for an aileron that spans 30% of the semi-wing, the chord should take up about 25% of the wing section chord. Sweep is mostly introduced for aerodynamic reasons, increasing the velocity at, which shockwaves are observed on the wing. However, a swept-back wing tends to have a higher divergence speed than an unswept wing [37]. No large sweep is necessary, mainly because in the expected velocity regime, shockwaves are not expected to occur. Also, a low sweep increases the general efficiency of the wing by attaining a high aspect ratio at a similar span.

The design process done in Ref. [16] focused mainly the internal structure of the wing and the set up of a simulation framework that could potentially optimise the system for a desired objective. Therefore, the dimensions of other structures were fully determined by rough estimations. The size ratios of the AP-3 kite are used to calculate the surface dimensions. However, these ratios were not provided by Ampyx Power.

Table 3 shows the determined design parameters. The stability of the aircraft is monitored closely throughout the simulations to make sure the aircraft can perform its pumping cycle and small corrections were made accordingly.

Table 4
Semi-wing detailed planform description at the root, rib locations and the tip.

LE Y_B m	TE Y_B m	Chord m	Twist °	$d_{x,\ sweep}$ m
0	0	4.4640	5	0
0.2	0.2	4.4640	5	0
1.0091	1.0091	4.4640	5	0
1.9182	1.9182	4.4640	5	0
2.8273	2.8273	4.4640	5	0
3.7361	3.9369	4.4623	4.9375	−0.00088
4.6469	4.845	4.4051	4.9376	−0.01679
5.5515	5.9632	4.2853	4.6987	−0.047491
6.4679	6.8681	4.1635	4.4374	−0.079494
7.3693	7.7825	4.0381	4.1770	−0.11097
8.2865	8.6868	3.9108	3.9191	−0.14300
9.1874	9.5751	3.7858	3.6581	−0.17446
10.1046	10.4794	3.6588	3.4034	−0.20649
11.0056	11.3676	3.5340	3.1459	−0.23795
11.9228	12.2719	3.4072	2.8948	−0.26998
12.7228	13.0607	3.2965	2.6192	−0.30145
13.7409	14.0645	3.1561	2.3947	−0.33348
14.6419	14.9528	3.0318	2.1332	−0.36494
15.5591	15.8571	2.9054	1.8665	−0.39697
16.4600	16.7453	2.7813	1.5954	−0.42843
17.3773	17.6496	2.6551	1.3295	−0.46046
18.2782	18.5379	2.5311	1.0593	−0.49192
19.1954	19.4422	2.4050	0.7942	−0.52395
19.9955	20.2310	2.2950	0.5184	−0.55542
21.0136	21.2347	2.1551	0.2604	−0.58745

Table 4 shows a detailed description of the wing planform necessary in combination with Table 3 to reconstruct the wing. Each 'leading edge(LE) Y_B' position is measured from the root in spanwise direction along the Y_B axis. The chord length is the (rotated) length of the rib at the specified position. The twist is the structural rotation of the airfoil sections in order to achieve higher angles of attack at the root and lower at the tip to reduce the lift-induced drag and increase the buckling load. Another benefit from this is to make sure the root stalls before the tip. This makes sure the ailerons can still function properly when the first signs of stall are present [38]. $d_{x,\ sweep}$ is the distance to the leading edge of the rib along the X_B axis, each rib is moved backwards to account for sweep and is measured from the unswept leading edge position. Rot_z is the rotation of the rib to become perpendicular to the trailing edge(TE). The trailing edge is swept forward to increase the aspect ratio of the wing.

3.2. Wing skin

The composite layup of the wing skin panels are designed for the root and tip sections, while interpolating linearly between them to eight sections. This is done by assigning a number of spanwise skin panels, one determined between two consecutive ribs, to each of the eight sections. Whenever the number of panels cannot be divided by eight, the number of panels is sorted in descending order from root to tip, allowing for more panels with higher thickness at the root. The number of layers are then determined by an optimisation procedure.

For each skin panel the layup consists of a $[45°_N, -45°_N, 45°_N, 0°_N]$ ply orientation, where N denotes the number of layers. Table 5 shows the MSC Nastran (software) material properties used for each layer.

Fig. 9 shows the distribution of the layup thickness over the wingspan of the top skin. Fig. 10 shows the distribution of the layup thickness over the wingspan of the bottom skin.

On both surfaces, top and bottom, it can be noted that the thicknesses increases when moving from the tip to the root, which one may expect. This comes from the bending moment that increases significantly towards the root. In other words, the composite plies have to withstand a higher loading and thus must be stronger. Because of the linear interpolation method between the root and the tip, no local buckling phenomena can be noted. On the bottom surface is can be clearly seen that the wingbox takes up most of the loads acting on the wing. Also on the top it can be seen that the wingbox has the highest thicknesses. The increased thicknesses present on the rear part of the wing are most likely occurring due to twist in the wing.

Table 5
MSC Nastran material properties of the 45°and the 0°UD plies.

Parameter	±45° fabric	UD 0° tape	Unit
Material type	MAT8	MAT8	-
Layer thickness	0.0002	0.00017	m
$E_{1,\ longitudinal}$	3.83×10^{10}	1.12×10^{11}	Pa
$E_{2,\ lateral}$	3.83×10^{10}	6.9×10^{9}	Pa
ν_{12}	0.3	0.3	-
G_{12}	4.70×10^{9}	9.9×10^{9}	Pa
G_{1Z}	4.70×10^{9}	9.9×10^{9}	Pa
G_{2Z}	2.35×10^{9}	4.9×10^{9}	Pa
ρ	1600	1600	$kg\,m^{-3}$
$A_{1,\ thermal}$	0	0	K^{-1}
$A_{2,\ thermal}$	0	0	K^{-1}
T_{ref}	0	0	K
X_t	8.88×10^{8}	2.10×10^{9}	Pa
X_c	8.88×10^{8}	1.73×10^{9}	Pa
Y_t	8.03×10^{8}	56.5×10^{6}	Pa
Y_c	8.18×10^{8}	56.5×10^{6}	Pa
S	1.07×10^{8}	1.02×10^{8}	Pa

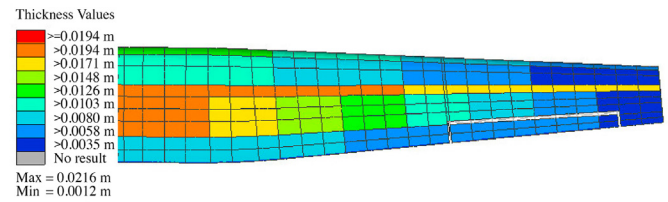

Fig. 9. Top skin layup thickness distribution [16].

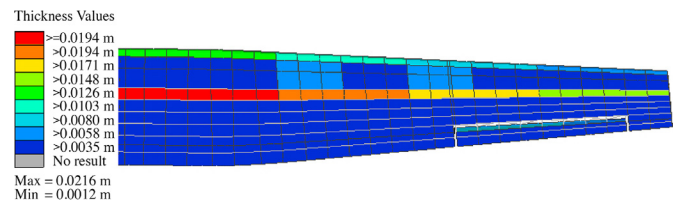

Fig. 10. Bottom skin layup thickness distribution [16].

3.3. Kite aerodynamics

For simplicity, it is chosen to use pre-computed static aerodynamic coefficients to determine the aerodynamic forces and moments. The wing and tail surfaces are calculated separately and summed. The forces (and moments) generated by the fuselages are neglected. However, the fuselages are taken into account for the determination of the kite's centre of gravity.

The wing's aerodynamic properties are determined using the FSI algorithm described in Ref. [26]. The three-dimensional wing is analysed between the minimum and maximum angles of attack of the linear regime in the lift versus angle of attack curve. The computation of these angles is described in Ref. [16]. The calculated lift and drag coefficients are shown in Fig. 11. The angle of attack is the angle between the relative flow velocity at the aircraft, also denoted as apparent wind velocity, and the X_B-axis of the body-fixed reference frame, which is aligned with the fuselages. The low maximum angle of attack is caused by the wing twist and a not optimal performing airfoil design. The pitch moment coefficient versus angle of attack is also given in Fig. 11. The roll coefficient at maximum aileron deflection (±35°) is also pre-computed by the FSI algorithm. The controller assumes a deflection between 1 and -1. The amplitude is then damped by the roll rate and then multiplied by the maximum roll coefficient (0.1424 [-]).

The aerodynamic properties of the elevator and rudder are also determined by pre-computed coefficients presented in Fig. 12. However, for these control surfaces, only the lift and drag are used, the pitch moment is neglected and the coefficients are not determined by the FSI algorithm but by using RFoil [39] and corrected for three-dimensional effects using the aspect ratio and lift-induced drag. The elevator and rudder are all moving tail surfaces. The angle of attack for the rudder is different than for the wing and elevator. For the rudder, this angle is assumed to be the sideslip angle. RFoil estimations are done for the NACA-0012 airfoil at a velocity of 60 m s^{-1} and a Reynolds number of 6×10^6.

4. Results

In this section the results from several pumping cycles are shown. At each data point in Fig. 20, optimisations were performed

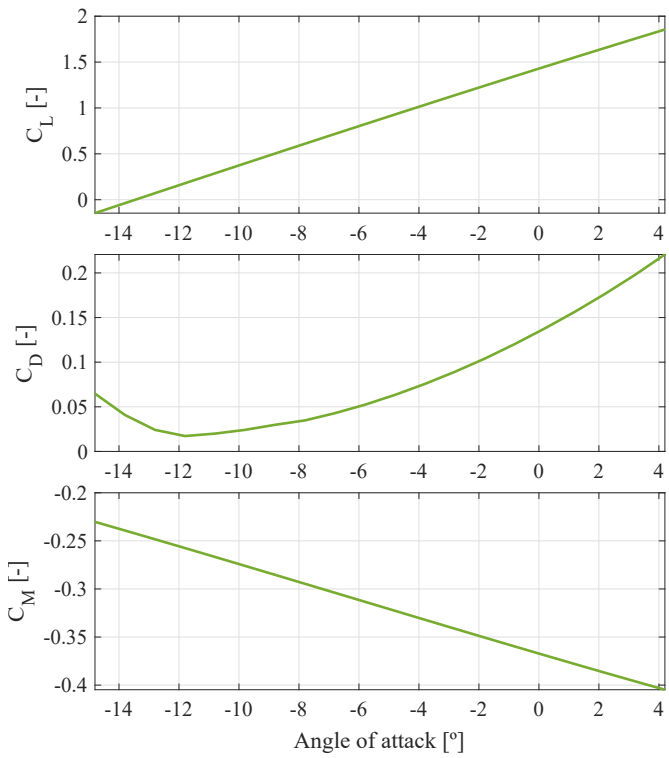

Fig. 11. Lift (top), drag (middle) and pitch moment (bottom) coefficient (wing) versus angle of attack.

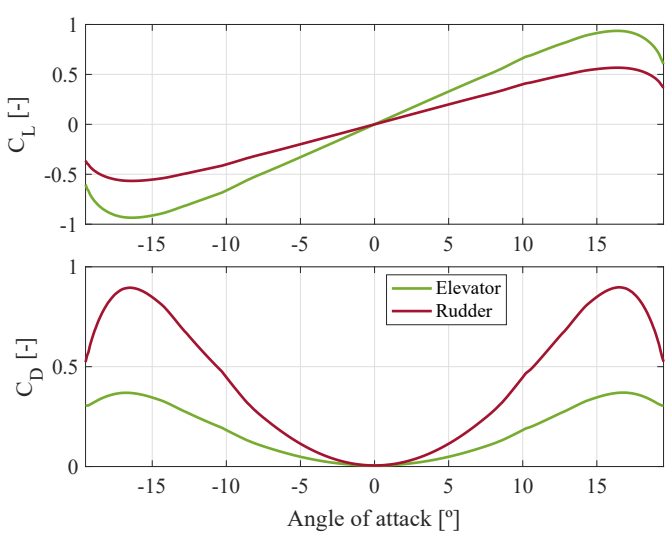

Fig. 12. Lift (Top) and drag (bottom) coefficient (elevator and rudder) versus angle of attack (side slip angle for the rudder).

for the parameters and strategy given in section 2.6. All shown results here are taken at 22 m s^{-1} maximum wind speed ($V_{w,\,250}$) unless stated otherwise.

4.1. Convergence criteria

The results presented in this section are all for a converged simulation. Convergence is achieved when the difference in average cycle power, between two consecutive pumping cycles, is lower than a prescribed threshold and a minimum of three pumping cycles are performed. The threshold increases with every cycle flown, as an increase in flown cycles also indicates a stable set of simulation parameters but might have a slightly higher difference between pumping cycles. Equation (28) shows the increase of the power threshold. With a minimum of three cycles, the threshold starts at 130 kW and increases then each pumping cycle with 43.3 kW. Convergence is measured at the end of the retraction phase. When convergence is met, the simulation stops and the results are taken for the last flown pumping cycle.

$$\text{Threshold} = \frac{130}{3} \cdot \text{N}^{\underline{o}}\ \text{cycles} \quad [\text{kW}]. \tag{28}$$

4.2. Pumping cycle

Fig. 13 illustrates the instantaneous mechanical power over a complete pumping cycle. During the figure-of-eight manoeuvres, the system loses power in upwards flight due to a short reel-in of the tether to counteract gravity. As the current kite is still relatively heavy, the winch retracts quickly to compensate for the loss in tension. On average, the system produces a mechanical power of 3.6 MW.

The theoretical peak cycle power of kites flying crosswind manoeuvres at an elevation angle β is calculated using Equation (29) with the values given in Table 6. This equation is Loyd's peak power [40] with additional cosine losses [41].

$$P_{\max} = \frac{4}{27} P_w A \frac{C_L^3}{C_{D,\text{eff}}^2} \cos^3\beta, \tag{29}$$

where $P_w = \frac{1}{2}\rho V_w^3$ is the wind power density, $C_L^3/C_{D,\text{eff}}^2$ is the non-dimensional force ratio during reel-out and $C_{D,\text{eff}}$ is given by Equation (30). This ratio, when not taking the tether into account, is also known as the climb factor in aircraft performance [42].

$$C_{D,\text{eff}} = C_{D,\text{kite}} + \frac{C_{d,\ \text{cyl}} l_{\text{tether}} d_{\text{tether}}}{4\,A}. \tag{30}$$

The aerodynamic curves from Fig. 11 combined with the logged

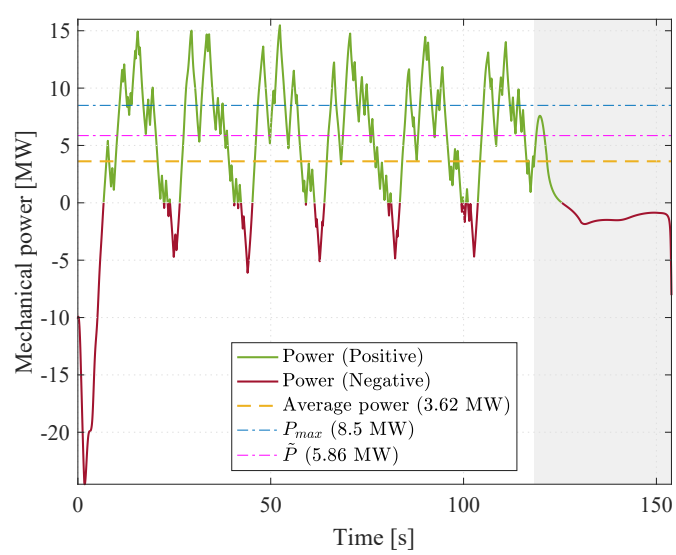

Fig. 13. Instantaneous mechanical cycle power at $V_{w,\,250} = 22$ m s^{-1}, including average power and the outcome of Equations (29) and (31). The grey area marks the reel-in phase.

Table 6
Loyd and Costello et al. parameters.

Parameter	Value	Unit
Wind power density (P_w)	6.52×10^3	$W\,m^{-2}$
Kite surface area (A)	150.45	m^2
Effective drag coefficient ($C_{D,eff}$)	0.2454	-
Lift coefficient (C_L)	1.76	-
Tether length (l_{tether})	797.2	m
Elevation angle (β)	30	°
Peak power without tether (P_{max})	15.5	MW
Peak power with tether (P_{max})	8.50	MW
Efficiency factor (e)	0.51	-
Maximum power harvesting factor (ζ)	11.6	-
Restrictive average power ($\tilde{P}$)	5.86	MW

angle of attack values during the traction phase of the converged pumping cycle are used to calculate the position where maximum $C_L^3/C_{D,eff}^2$ occurs during the traction phase of a converged pumping cycle. The maximum ratio with tether drag happens at a different simulation time than without. The peak power calculated by Equation (29) is higher than the simulated peak power when not taking the tether into account. However, when approximating the influence of tether drag on C_D, which is shown by Equation (30), the peak power is expected to be lower. Equation (29) predicts the maximum power that theoretically can be achieved. Therefore, normally one would expect a lower peak power from the simulation than predicted. Tether drag is taken into account during simulations and thus can be seen that the simulations have a higher peak power than expected. However, the difference can be explained by the dynamic effects of gravity, which are not taken into account by Loyd. The peak power occurs during a downwards flight, which supports this statement and can also be observed in Fig. 17.

Another theoretical comparison is made by following the approach of Costello et al. [43]. Equation (31) shows the analytical relation of the restrictive average power for a generic kite system.

$$\tilde{P} = eP_W A\zeta, \tag{31}$$

where $\tilde{P}$ is the restrictive (upper boundary) on average power a generic kite system could produce, ζ is the maximum power harvesting factor given by Equation (32) and e is the efficiency factor given by Equation (33).

$$\zeta = \frac{4}{27}\left[\frac{C_L^3}{C_{D,eff}^2}\right]_{average}. \tag{32}$$

$$e = \cos^3\left[\beta + \sin^{-1}\left(\frac{\text{norm } F_{drag}}{\text{norm } F_{aero}}\sin\beta + \frac{mg}{\text{norm } F_{aero}}\cos\beta\right)\right], \tag{33}$$

where

The simulated average power is indeed lower than the upper boundary calculated analytically using the values in Table 6. The main difference comes from the power loss during reel-in, which is not taken into account analytically but is taken into account from the simulation results. Small errors occur due to the averaging of aerodynamic forces as well as the elevation angle, which is assumed constant.

Fig. 14 shows both the continuous tether force and reel-out speed. For a better understanding, the maximum allowable tether force and the tracked set-point is shown in the same graph. It is clearly visible that the winch controller has problems tracking the set-point. This is one of the difficulties when using a relatively simple controller. The previously mentioned power loss effect during figures of eight is shown by the reel-out speed.

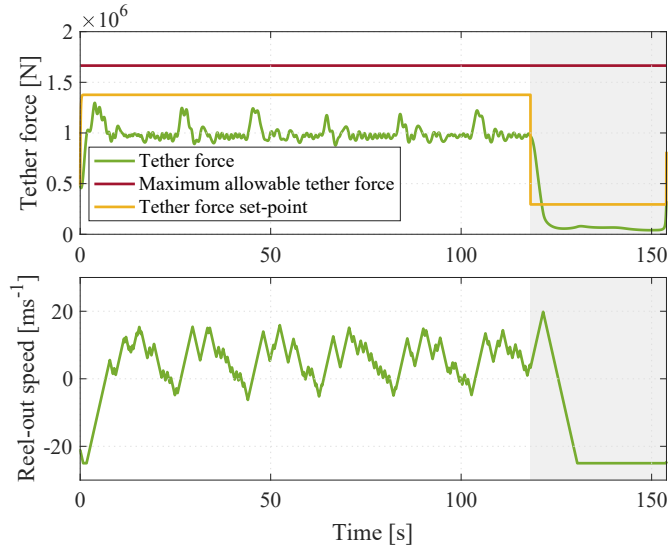

Fig. 14. Tether force magnitude at the kite (top) and the reel-out speed (bottom) at $V_{w,250} = 22$ m s^{-1}. The grey area marks the reel-in phase. Please note that the reel-in phase is determined by the flight state, not the (negative) value of the reel-out speed.

During the retraction phase, there is a low tension kept on the tether. This is necessary to prevent snapping when transitioning back into traction. This way the dynamics between the kite and the tether are better synchronised to prevent a rupture. During early point-mass simulations similar to Ref. [20], this effect was not observed as the aircraft's response was much faster due to the lack of inertia. Optimisations performed for the point-mass system, therefore, result in a more sagging tether during retraction, minimising the tether force and thus minimising the loss of power.

Fig. 15 shows the apparent wind speed, the angle of attack and the sideslip angle the kite endures during its pumping cycle. Fig. 16 gives an insight in the lift over drag ratio during flight. As this pumping cycle is a result of power optimisations it can be clearly seen that in order to maximise power, the kite prefers high lift (maximum angle of attack) during traction. This disregards the effect that aerodynamic drag is significantly higher, lowering the L/D. During retraction the kite pitches to the angle of attack where high lift over drag occurs creating a more effective glide ratio back towards the ground station. Due to the phenomena around tether snapping, this effective glide ration cannot be maintained during the whole retraction phase. Fig. 16 also shows the tether length, the small moments of retraction during figure-of-eight flight are visible together with the shortcoming of the winch controller. When the retraction phase is initiated, characterised by the sudden increase in kite lift over drag, the tether is still reeling-out. Part of this is caused by the dynamic effects of the winch (e.g. inertia) but the other part by the current control approach. These effects can be seen in opposite direction at the start of the pumping cycle, where the tether is still reeling in even though the traction phase is initiated. This results in the highest negative peak of power.

4.3. Flight paths

In Section 2.6 different parameters that have an influence on the flight path are presented, which are varied during optimisations. This way the flight path strategy is only prescribed; traction phase consists of figures of eight at an elevation angle and during

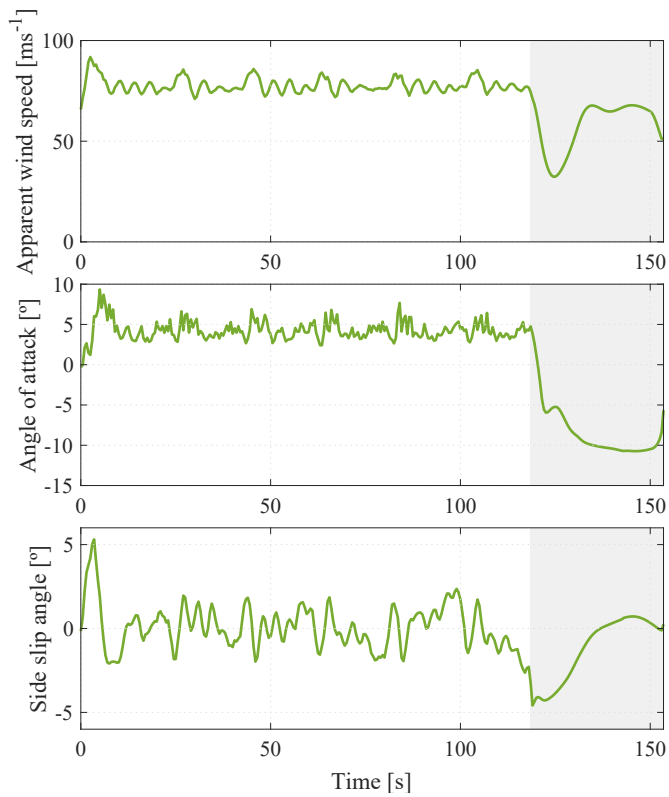

Fig. 15. Apparent wind speed (top), the angle of attack (middle) and the sideslip angle (bottom) at $V_{w,\,250} = 22$ m s^{-1}. The grey area marks the reel-in phase.

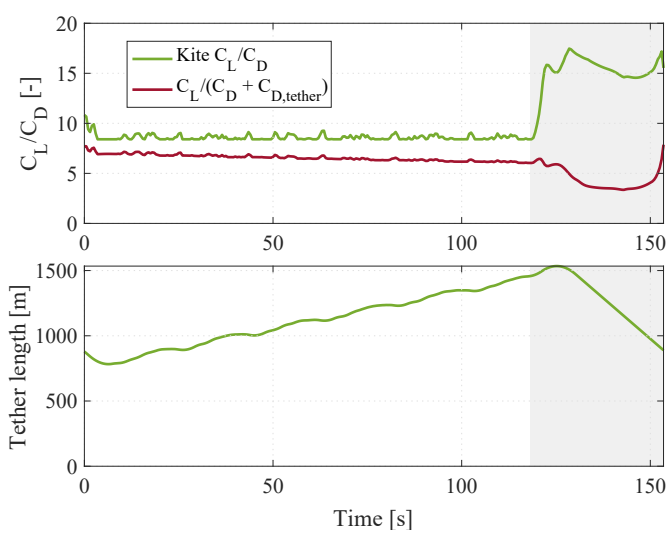

Fig. 16. Glide ratio, C_L/C_D (top), and tether length (bottom) at $V_{w,\,250} = 22$ m s^{-1}. The grey area marks the reel-in phase.

retraction an arc is flown back towards the ground station at the outer edge of the figure of eight. Transition from traction to retraction occurs at maximum tether length and the transition back to traction occurs when the kite passes the x_W (wind reference frame) position of the retraction target. Then the optimisation algorithm is free to change the flight path by alternating the geometry and position in space. The path resulting from the optimisation performed at $V_{w,250} = 22$ m s^{-1} is illustrated in Fig. 17, which is coloured by the continuous power production. The statement made

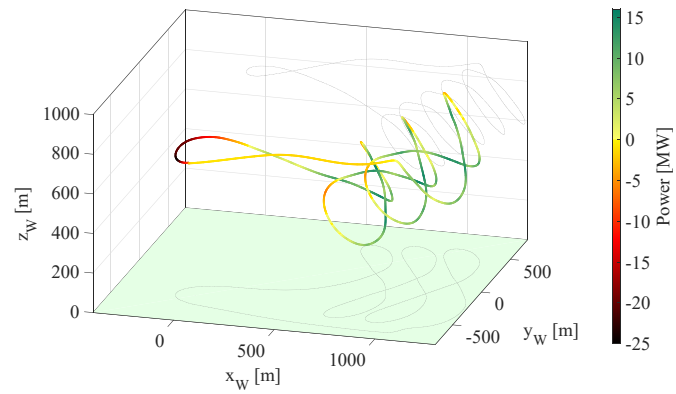

Fig. 17. Optimised flight path at $V_{w,\,250} = 22$ m s^{-1} including the power production at each stage.

in Section 4.2 about the tether force being kept during retraction can be clearly seen now. The power production is negative during this phase due to the tether force (always positive) and the negative reeling speed. Also the loss of power during upwards flight (reel-in to counteract the loss in tether force due to gravity) at the outer edges of the figure-of-eight can be observed.

The influence of wind speed on the resulting flight path is shown in Fig. 18. At very low wind speeds the system has difficulties producing power. The lower wind speed decreased the aerodynamic force magnitudes, lowering the tension force. The winch controller tracks the tether force, meaning when the pulling force is not high enough, it slows down the reel-out speed resulting in a much more densely packed number of figures of eight than at a higher wind speed. At a wind speed of 30 m s^{-1} the system is limited during traction by the maximum tether force but loses more power during retraction. This has the effect that the retraction phase is kept short compared to lower wind speeds. Another effect of the high wind speed is on the controllability of the kite; it becomes much harder to perform the required manoeuvres when the tension force on the tether cannot be increased due to tether rupture prevention.

A final comparison is made between optimisations for the point mass assumption (3DoF) and a rigid body dynamic kite (6 DoF) illustrated in Fig. 19. Both optimisations were performed using the same limits and wind speed. It is clearly visible that the point-mass kite can perform more thin and compact figures of eight. A more

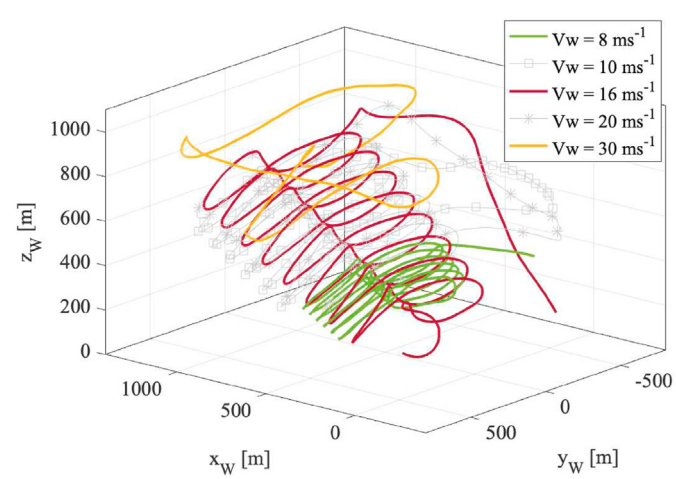

Fig. 18. Optimised flight paths at different maximum wind speeds.

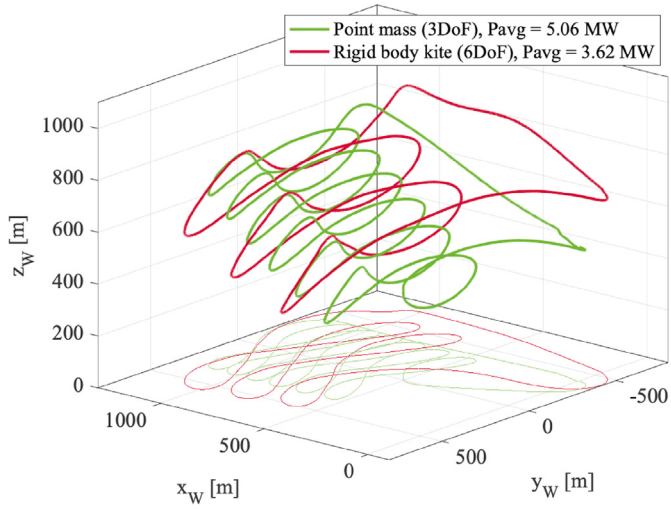

Fig. 19. Optimised flight paths at $V_{w,\,250} = 22$ m s^{-1} including the power production at each stage for both 6 DoF and 3DoF simulations.

efficient course is flown, which results in a higher average power for the pumping cycle. Especially the steeper slope during the retraction phase contributes to less power loss due to more tether sag and thus lower tension forces. The point-mass assumption neglects the kite's inertia, making it easier to prevent tether rupture (snapping) when transitioning from retraction into the traction phase.

4.4. Power curve

The outcome of different optimisations at a range of wind speeds between 8 and 30 m s^{-1} can be found in Fig. 20. In the beginning, similar to conventional wind turbines, the power seems to follow a cubic relation with respect to wind speed. This could also be expected from Loyd's theoretical equations. However, from about 20 m s^{-1} the curve flattens to a maximum and increasing the wind speed further would even decrease the average power produced over a pumping cycle. As described at the end of Section 4.3,

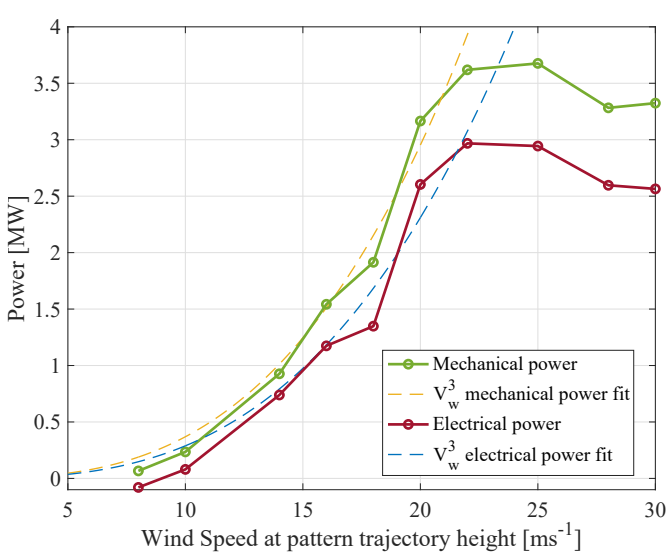

Fig. 20. Power curve containing both the average mechanical and electrical pumping cycle power at different maximum wind speeds. The wind speed at 100 m altitude is also shown for comparison.

this is caused by the retraction phase. A perfect gliding flight cannot be maintained during retraction as tension is required to be on the tether when transitioning back to traction to prevent it from rupturing when the tether suddenly straightens from a large sagging condition. A small sag will occur however the tether tension at the ground station is kept higher than zero. This causes an increase in power loss during reel-in with increasing wind speed. As the power produced during traction is limited by the maximum tether force, the curve cannot continue to follow the cubic relation. Another effect on this curve would be the generator rated power, however, this is not taken into account in this work. To illustrate the cubic law, a cubic fit to the data between 8 and 20 m s^{-1} is also shown in Fig. 20. The simulation only determines the mechanical power. In order to approximate the electrical power from converting mechanical power, Equation (34) is used [44]. The generator, motor and battery efficiencies of Table 7 are taken into account. The power during reel-out $P_{m,\,o}$ is averaged over the full pumping cycle. The same is done for the power produced during reel-in $P_{m,\,i}$, which is negative. During reel-out, only the generator efficiency is applied. During reel-in, the power comes from a battery where it was previously stored and then the tether is retracted by a motor, which therefore requires two efficiencies. The maximum electrical power is approximately 3 MW.

$$P_e = P_{m,\,o_{avg}}\eta_g + \frac{P_{m,\,i_{avg}}}{\eta_m \eta_b} \tag{34}$$

5. Conclusions and outlook

The reference kite and simulation framework presented in this work are a big step toward a fully open-source benchmark for Ground-Gen airborne wind energy systems by operating in pumping cycles. Whether one uses these simulations to cross-reference results or to further improve sub-components of the system, this framework can provide a solid starting base for more realistic simulations—accelerating developments for a more renewable future based on airborne wind.

The most important details of a large-scale multi-megawatt Airborne Wind Energy reference aircraft, simulation framework and power optimisation strategy are presented. The simulation framework consists of a dynamic system model, which couples the airborne system (e.g. kite aerodynamics and control), a quasi-static tether model, ground station and environmental physics. Possible flight paths are given for the reference kite at different wind speeds to produce megawatt power. The quasi-static tether model allows stiff tether materials to be used during fast simulations of an airborne wind energy system.

The power curve shows very similar behaviour to regular wind turbines at lower wind speeds. At higher wind speeds, the retraction phase costs more power and thus an optimal wind speed can be obtained for maxim power. Maximum mechanical power of 3.6 MW is found, and including conversion losses of the electrical drive train the maximum electrical power is estimated at 3 MW.

The current results outline the potential of a 150 m^2 wing, which is able to generate multiple megawatts of power. However, the

Table 7
Electrical power efficiencies [44].

Parameter	Value
Generator efficiency (η_g)	90%
Motor efficiency (η_m)	90%
Battery efficiency (η_b)	95%

current winch controller has difficulties tracking the tether force set-point. Therefore, during traction, the average tension force is lower than what the tether could withstand. Changing the winch model itself could also improve the tether force behaviour. If a more realistic physical representation of the winch is implemented (e.g. inertia, drum size, generator efficiencies), the controller might respond better, causing the results to approach reality more closely. Another method for improving the winch response is to change the control strategy altogether, away from only tether force tracking and include reel-out speed tracking, for example. This could result in more quiet and stable system behaviour.

A small comparison with point mass dynamics shows the importance of simulating a rigid body kite when looking at flight path optimisations. More realistic power output estimations require more detailed flight dynamics. For the current rigid body kite flying an optimised flight path, experiencing a maximum wind speed of 22 m s^{-1}, the average mechanical power is 28.5% less than its point-mass counterpart. This reduction can be directly derived back to the effects of inertia. Assuming point-mass dynamics instead of a rigid body, allows for a more efficient flight path. Steeper retraction slopes can be flown, allowing for a shorter retraction phase and lower tether force. Including inertia, results in a flight path with lower tether sag. This increases the retraction time and tether force and thus larger power consumption.

It must be noted that optimisations in this work are steered in a particular direction by choosing the set of parameters to optimise and in what range. As the current work focused on producing useful results at low computational cost, not all controller and system parameters were included in the optimisation. Increasing the number of optimisation variables, should lead to different results with the potential of increasing average power production of pumping cycles. Also the reference design of the kite is not optimal. Early structural optimisations were done to get to this design, but many things were not considered yet. The lift over drag performance of this aircraft is not very high; combining this with the fact that the kite is quite heavy, the performance of this kite is not meant to compete with conventional wind energy but does succeed as a perfect starting point for further research on large-scale airborne wind energy systems.

Ongoing work examines the behaviour of the system when using a higher fidelity aerodynamic model, taking into account fluid-structure-interaction. However, continuing the developments of the reference framework on all aspects are key in making this the AWE benchmark like the NREL 5 MW wind turbine is for the conventional wind energy industry.

Data availability

Both rigid body and point-mass simulation models, including all controller algorithms and the reference design of the kite is available from Refs. [23,32] in open-access. Setting the degrees of freedom to 6, and the wind speed to 22 m s^{-1} results in a simulation output similar to the data used in this paper. This framework can be used for benchmarking and cross-validation of alternative simulation frameworks developed by the sector.

CRediT authorship contribution statement

Dylan Eijkelhof: Conceptualization, Methodology, Software, Writing – original draft, preparation and creation, Writing – review & editing. **Roland Schmehl:** Supervision, Writing – review & editing, Funding acquisition.

Declaration of competing interest

The authors declare the following financial interests/personal relationships which may be considered as potential competing interests: Dylan Eijkelhof reports financial support was provided by European Regional Development Fund.

References

[1] M. Diehl, R. Leuthold, R. Schmehl (Eds.), The International Airborne Wind Energy Conference, University of Freiburg & Delft University of Technology, Freiburg, Germany, 2017, https://doi.org/10.6094/UNIFR/12994, 2017: Book of Abstracts.

[2] R. Schmehl, O. Tulloch (Eds.), The International Airborne Wind Energy Conference, University of Strathclyde, Glasgow, United Kingdom, 2019, https://doi.org/10.4233/uuid:57fd203c-e069-11e9-9fcb-441ea15f7c9c, 2019: Book of Abstracts.

[3] P. Jamieson, Innovation in Wind Turbine Design, 2 ed., John Wiley & Sons, Hoboken, NJ, 2018 https://doi.org/10.1002/9781119137924.

[4] V. Nelson, Innovative Wind Turbines: an Illustrated Guidebook, CRC Press, Boca Raton, FL, 2019, https://doi.org/10.1201/9781003010883.

[5] P. Weiss, After highflyer crashes, airborne wind energy regroups, Engineering 7 (2021) 277–279, https://doi.org/10.1016/j.eng.2021.01.004.

[6] C. Vermillion, M. Cobb, L. Fagiano, R. Leuthold, M. Diehl, R.S. Smith, T.A. Wood, S. Rapp, R. Schmehl, D. Olinger, M. Demetriou, Electricity in the air: insights from two decades of advanced control research and experimental flight testing of airborne wind energy systems, Annu. Rev. Control (2021), https://doi.org/10.1016/j.arcontrol.2021.03.002.

[7] M. Diehl, Airborne wind energy: basic concepts and physical foundations, in: U. Ahrens, M. Diehl, R. Schmehl (Eds.), Airborne Wind Energy, Green Energy and Technology, Springer, Berlin Heidelberg, 2013, pp. 3–22, https://doi.org/10.1007/978-3-642-39965-7_1.

[8] L. Larco, P. Echeverri, Makani M600 - Makani flight simulator, URL: https://github.com/google/makani, 2020. (Accessed 20 February 2021).

[9] J. Wijnja, R. Schmehl, R.D. Breuker, K. Jensen, D. Vander Lind, Aeroelastic analysis of a large airborne wind turbine, J. Guid. Control Dynam. 41 (2018) 2374–2385, https://doi.org/10.2514/1.G001663.

[10] F. Bauer, Multidisciplinary Optimization of Drag Power Kites, Ph.D. thesis, Technische Universität München, 2021.

[11] P. Williams, Cable modeling approximations for rapid simulation, J. Guid. Control Dynam. 40 (2017) 1779–1788, https://doi.org/10.2514/1.G002354.

[12] G. Licitra, J. Koenemann, A. Bürger, P. Williams, R. Ruiterkamp, M. Diehl, Performance assessment of a rigid wing airborne wind energy pumping system, Energy 173 (2019) 569–585, https://doi.org/10.1016/j.energy.2019.02.064.

[13] G. Licitra, A. Bürger, P. Williams, R. Ruiterkamp, M. Diehl, Aerodynamic model identification of an autonomous aircraft for airborne wind energy, Optim. Control Appl. Methods 40 (2019) 422–447, https://doi.org/10.1002/oca.2485.

[14] S. Rapp, R. Schmehl, E. Oland, T. Haas, Cascaded pumping cycle control for rigid wing airborne wind energy systems, J. Guid. Control Dynam. 42 (2019) 2456–2473, https://doi.org/10.2514/1.G004246.

[15] S. Rapp, R. Schmehl, E. Oland, S. Smidt, T. Haas, J. Meyers, A modular control architecture for airborne wind energy systems, in: Proceedings of the AIAA Scitech 2019, California, San Diego, 2019, pp. 1–25, https://doi.org/10.2514/6.2019-1419.

[16] D. Eijkelhof, Design and Optimisation Framework of a Multi-MW Airborne Wind Energy Reference System, Master's thesis, Delft University of Technology & Technical University of Denmark, 2019. URL: http://resolver.tudelft.nl/uuid:e759f9ad-ab67-43b3-97e0-75558ecf222d.

[17] M. Kruijff, R. Ruiterkamp, A roadmap towards airborne wind energy in the utility sector, in: R. Schmehl (Ed.), Airborne Wind Energy – Advances in Technology Development and Research, Green Energy and Technology, Springer, Singapore, 2018, pp. 643–662, https://doi.org/10.1007/978-981-10-1947-0_26.

[18] E.C. Malz, J. Koeneman, S. Sieberling, S. Gros, A reference model for airborne wind energy systems for optimization and control, Renew. Energy 140 (2019) 1004–1011, https://doi.org/10.1016/j.renene.2019.03.111.

[19] S. Rapp, R. Schmehl, Enhancing Control System Resilience for Airborne Wind Energy Systems through Upset Condition Avoidance, 2020 arXiv:2004.02730.

[20] D. Eijkelhof, S. Rapp, U. Fasel, M. Gaunaa, R. Schmehl, Reference design and simulation framework of a multi-megawatt airborne wind energy system, J. Phys. Conf. 1618 (2020), 032020, https://doi.org/10.1088/1742-6596/1618/3/032020.

[21] E.C. Malz, V. Verendel, S. Gros, Computing the power profiles for an airborne wind energy system based on large-scale wind data, Renew. Energy 162 (2020) 766–778, https://doi.org/10.1016/j.renene.2020.06.056.

[22] Elena C. Malz, Viktor Walter, Lisa Göransson, Sebastien Gros, The value of airborne wind energy to the electricity system, Wind Energy 25 (2) (2022) 281–299. https://doi.org/10.1002/we.2671.

[23] D. Eijkelhof, R. Schmehl, MegAWES - megawatt-scale airborne wind energy system, URL: https://github.com/awegroup/MegAWES, 2021. (Accessed 15 February 2021).

[24] B.L. Stevens, F.L. Lewis, E.N. Johnson, Aircraft Control and Simulation: Dynamics, Controls Design, and Autonomous Systems, John Wiley & Sons, 2015, https://doi.org/10.1002/9781119174882.
[25] S. Rapp, Robust Automatic Pumping Cycle Operation of Airborne Wind Energy Systems, Ph.D. thesis, Delft University of Technology, 2021, https://doi.org/10.4233/uuid:ab2adf33-ef5d-413c-b403-2cfb4f9b6bae.
[26] U. Fasel, P. Tiso, D. Keidel, G. Molinari, P. Ermanni, Reduced-order dynamic model of a morphing airborne wind energy aircraft, AIAA J. 57 (2019) 3586–3598, https://doi.org/10.2514/1.J058019.
[27] MathWorks Inc., Matlab R2019b Documentation: Equation Solving Algorithms, The MathWorks Inc., Natick, Massachusetts, 2019. URL: https://www.mathworks.com/help/releases/R2019b/optim/ug/equation-solving-algorithms.html.
[28] F. Bañuelos-Ruedas, C.Á. Camacho, S. Rios-Marcuello, Methodologies Used in the Extrapolation of Wind Speed Data at Different Heights and its Impact in the Wind Energy Resource Assessment in a Region, Wind Farm-Technical Regulations, Potential Estimation and Siting Assessment, 2011, pp. 97–114, https://doi.org/10.5772/20669.
[29] M. Schelbergen, P.C. Kalverla, R. Schmehl, S.J. Watson, Clustering wind profile shapes to estimate airborne wind energy production, Wind Energy Sci. 5 (2020) 1097–1120, https://doi.org/10.5194/wes-5-1097-2020.
[30] M. Sommerfeld, High altitude lidar measurements of the wind conditions for airborne wind energy systems, in: Presentation at the 2017 Airborne Wind Energy Conference, Freiburg, Germany, 2017. URL: https://awec2017.com/presentations/markus-sommerfeld.
[31] A. Auger, N. Hansen, Tutorial CMA-ES: evolution strategies and covariance matrix adaptation, in: Proceedings of the 14th Annual Conference Companion on Genetic and Evolutionary Computation, 2012, pp. 827–848, https://doi.org/10.1145/2330784.2330919.
[32] D. Eijkelhof, Megawes, Six-Degrees-Of-Freedom Simulation Model for Future Multi-Megawatt Airborne Wind Energy Systems, Delft University of Technology, 2021, https://doi.org/10.4121/17311523.
[33] M. Kruijff, R. Ruiterkamp, AP-3, a safety and autonomy demonstrator for utility-scale airborne wind energy, in: M. Diehl, R. Leuthold, R. Schmehl (Eds.), The International Airborne Wind Energy Conference 2017: Book of Abstracts, Freiburg, Germany, 2017, pp. 16–19. URL: http://resolver.tudelft.nl/uuid:53286eb3-3e58-4f33-accf-c80c4876a60a.
[34] J. Bosch, S. Sieberling, S. Wilhelm, Status update and review of the AP-3 development, in: R. Schmehl, O. Tulloch (Eds.), The International Airborne Wind Energy Conference 2019: Book of Abstracts, Glasgow, UK, 2019, pp. 12–19. URL: http://resolver.tudelft.nl/uuid:1e49f8b0-a9a1-4883-81b0-abbc190a60dc.
[35] G. Licitra, Identification and Optimization of an Airborne Wind Energy System, Ph.D. thesis, University of Freiburg, 2018, https://doi.org/10.6094/UNIFR/16226.
[36] R.C.M. Chaitanya, M. Tarkian, C. Jouannet, Model based aircraft control system design and simulation, in: Proceedings of the 27th International Congress of the Aeronautical Sciences, ICAS, 2010, pp. 3338–3347. URL: http://www.icas.org/ICAS_ARCHIVE/ICAS2010/PAPERS/399.PDF.
[37] J. Wright, J. Cooper, Introduction to Aircraft Aeroelasticity and Loads, Aerospace Series, John Wiley & Sons, 2008, https://doi.org/10.1002/9781118700440.
[38] G.S. Kumar, S. Mohan, R.S. Rao, Design development and CFD simulation of a variable twist wing, Imper. J. Interdiscip. Res. 3 (2017), https://doi.org/10.13140/RG.2.2.29174.32323.
[39] R. Van Rooij, Modification of the Boundary Layer Calculation in Rfoil for Improved Airfoil Stall Prediction, 1996. Report IW-96087R TU-Delft, the Netherlands.
[40] M.L. Loyd, Crosswind kite power (for large-scale wind power production), J. Energy 4 (1980) 106–111, https://doi.org/10.2514/3.48021.
[41] R. Schmehl, M. Noom, R. van der Vlugt, Traction power generation with tethered wings, in: U. Ahrens, M. Diehl, R. Schmehl (Eds.), Airborne Wind Energy, Green Energy and Technology, Springer, Berlin Heidelberg, 2013, pp. 23–45, https://doi.org/10.1007/978-3-642-39965-7_2.
[42] G. Ruijgrok, Elements of Airplane Performance, Delft Academic Press, 2009. URL: https://www.delftacademicpress.nl/ae02.php.
[43] S. Costello, C. Costello, G. François, D. Bonvin, Analysis of the maximum efficiency of kite-power systems, J. Renew. Sustain. Energy 7 (2015), 053108, https://doi.org/10.1063/1.4931111.
[44] U. Fechner, R. Schmehl, Model-based efficiency analysis of wind power conversion by a pumping kite power system, in: U. Ahrens, M. Diehl, R. Schmehl (Eds.), Airborne Wind Energy, Green Energy and Technology, Springer, Berlin Heidelberg, 2013, pp. 249–269, https://doi.org/10.1007/978-3-642-39965-7_14.